Space: Science & Technology
A SCIENCE PARTNER JOURNAL

RESEARCH ARTICLE

Frequency-Sweeping Interferometry for Intersatellite Baseline Metrology in Array Telescope Formation

Wenjun Chen[1], Xiaoping Li[1], Zhongwen Deng[1*], Chenxu Wang[1], Shuwei Zhang[1], Haifeng Sun[1], Hengkang Zhang[2], Lin Li[2], Li Wang[2], Hai Gong[3], Herman Koara[4], Gleb Vdovin[5], and Weimin Bao[1,6]

[1]School of Aerospace Science and Technology, Xidian University, Xi'an 710071, China. [2]Space Optoelectronic Measurement and Perception Lab, Beijing Institute of Control Engineering, Beijing 100190, China. [3]Huzhou Research Institute of Zhejiang University, Zhejiang University, Huzhou 313000, China. [4]College of Control Science and Engineering, Zhejiang University, Hangzhou 310000, China. [5]Faculty of Mechanical Engineering, Delft University of Technology, 2628CD Delft, The Netherlands. [6]China Aerospace Science and Technology Corporation, Beijing 100048, China.

*Address correspondence to: zwdeng@xidian.edu.cn

Citation: Chen W, Li X, Deng Z, Wang C, Zhang S, Sun H, Zhang H, Li L, Wang L, Gong H, et al. Frequency-Sweeping Interferometry for Intersatellite Baseline Metrology in Array Telescope Formation. *Space Sci. Technol.* 2026;6:Article 0482. https://doi.org/10.34133/space.0482

Submitted 10 October 2025
Revised 4 December 2025
Accepted 19 January 2026
Published 4 March 2026

Space-based distributed array telescope formations hold substantial potential for deep space exploration, with their performance highly dependent on precise baseline measurements between subtelescopes. This study presents a double-sideband frequency-sweeping interferometry (DSB-FSI) technique based on electro-optic modulation for intertelescope baseline measurements. To address the lack of on-orbit frequency-sweep calibration references, a Fabry–Pérot etalon is used for real-time in situ frequency-sweep rate calibration. Experimental results show that the Fabry–Pérot etalon effectively calibrates the frequency-sweep rate of the DSB-FSI system, reducing long-term baseline measurement drift error from 20.11 to 13.38 μm and decreasing maximum measurement deviation from 18.03 to 13.14 μm over a 5.7-m baseline. Metrological calibration confirms that the calibrated system achieves a baseline measurement accuracy of 44.30 μm over a 10-m range, with excellent dynamic measurement performance for monitoring baseline variations. The DSB-FSI technique is expected to provide a reliable solution for the high-precision intertelescope baseline measurements in "MEAYIN" (Multiple-Spacecraft Exoplanet Aperture Synthetic Interferometer) project, thus supporting the advancement of space-based distributed array telescope formation technologies.

Introduction

Space-based distributed array telescope formations hold considerable importance and research interest in deep space exploration [1–3]. Through coordinated multitelescope observation and task allocation, these systems substantially enhance observational capabilities. The implementation of long-baseline optical interferometry enables high-precision tracking and characterization of space targets, providing critical technological support for early identification, orbital prediction, and defense strategies against hazardous objects such as small bodies, comets, and space debris [4]. Moreover, distributed array telescope formations offer substantial engineering potential for space exploration missions, including near-Earth planet exploration, solar physics research, and the search for extraterrestrial life [5].

In 2019, the China Aerospace Science and Technology Corporation initiated the "MEAYIN" (Multiple-Spacecraft Exoplanet Aperture Synthetic Interferometer) project [1], which proposes the development of a space-based distributed synthetic aperture telescope array for high-resolution direct imaging in deep space exploration. Within this telescope formation, the precise measurement of intertelescope baseline length serves as a fundamental requirement for maintaining multitier accurate control and stable configuration of the distributed telescope platform [6,7]. The measurement capability plays a critical role in determining the operational reliability of the entire formation.

Laser measurement technology is an ideal choice for space-based precision metrology due to its noncontact operation, high accuracy, and high resolution. Among various laser measurement techniques, frequency-sweeping interferometry (FSI) enables simultaneous high-precision measurement of absolute distance and dynamic characteristics by analyzing the beat signal between the frequency-modulated laser and its echo [8–10]. Compared to time-of-flight, multiwavelength interferometry, and optical frequency comb methods, FSI offers advantages such as high accuracy, unambiguous, and compact structure, making it a promising approach for future space exploration missions. Although FSI holds marked technical advantages

[11–14], it remains constrained by 2 major challenges: (a) frequency-sweep nonlinearity in the tunable laser [9,12,15] and (b) dynamic error amplification effect [10,16,17].

In our previous work, although some advances have been made in addressing these 2 major issues [6,13,18], the simultaneous suppression of both frequency-sweep nonlinearity and dynamic error amplification remains a critical technical challenge. It has been demonstrated that electro-optic modulation based on lithium niobate waveguides enables the transfer of a linearly chirped radio frequency (RF) signal onto a stabilized laser carrier, thereby generating highly linear frequency-sweep sidebands [19]. Furthermore, by using a Mach–Zehnder modulator (MZM), 2 strictly synchronized, linearly modulated sidebands with opposite frequency-sweep directions can be produced on either side of the stabilized laser spectrum [20–23]. This double-sideband FSI (DSB-FSI) system not only achieves highly linear frequency sweeps but also effectively suppresses dynamic error amplification.

The DSB-FSI system offers high component maturity and is well suited for miniaturized and integrated designs, making it suitable for aerospace measurement applications. However, current DSB-FSI systems lack a stable traceable reference for frequency-sweep calibration, which limits the on-orbit measurement accuracy and long-term stability. Although techniques such as gas absorption cells [24], optical frequency combs [25], and auxiliary reference interferometers [26] can serve as traceable references for FSI systems, their high cost and system complexity hinder their use in aerospace on-orbit applications. To address this limitation, we propose a DSB-FSI system utilizing a Fabry–Pérot (F–P) etalon as a traceable reference. Furthermore, we derive the theoretical expression for the F–P resonance signals generated by the double-sideband frequency-sweep laser within the F–P etalon. Experimental results demonstrate that using an F–P etalon as the frequency-sweep rate calibration reference effectively suppresses long-term distance drift errors caused by frequency-sweep instability.

Materials and Methods

System design and measurement principle

Figure 1 illustrates the schematic of the space-based distributed array telescope formation proposed in the "MEAYIN" project. In space-based optical interferometric imaging tasks, the formation must satisfy coplanar (locating within the same plane), cophased (having fixed phase positions), and codirectional (pointing in the same direction) configuration requirements. Consequently, high-precision intertelescope baseline measurement is essential for the stable operation for this formation. This section presents the system design and baseline measurement principles of the DSB-FSI system.

DSB-FSI system design

The schematic diagram of the DSB-FSI system equipped with an F–P etalon is illustrated in Fig. 2. A narrow-linewidth laser at 1,550 nm serves as the laser source. An electro-optic modulator with a dual Mach–Zehnder structure is used, and the detailed modulation principle is shown in Fig. 2B. To obtain positive and negative frequency-sweep sidebands, the linear frequency-modulated RF signal is amplified and then injected into the MZM, where it is divided into 2 paths with a 90° phase shift. Meanwhile, 3 dc signals are applied to the MZM to precisely adjust its phase [27,28]. The RF signal is generated by a commercial frequency-sweep source.

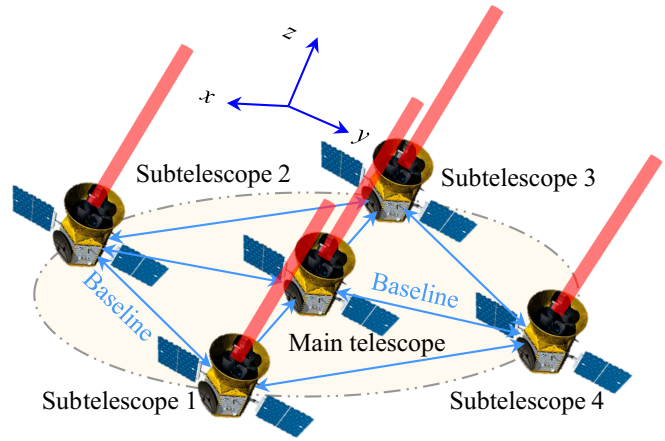

Fig. 1. The schematic diagram of the space-based distributed array telescope formation in the "MEAYIN" project.

For both sidebands, the bandwidth is nearly 8 GHz, and the sweep time is 1 ms. Subsequently, the double-sideband modulated laser is split into 2 paths by fiber splitter 1 (FS1). One path passes through collimator 2 (COL2) and enters the F–P etalon, where the F–P resonance signals are generated. The other path is further divided into emitted and reflected beams at FS2. The reflected beam enters the circulator, is coupled into free space via COL1, and, after being reflected by the target, reenters the circulator. Finally, the reflected beam interferes with the emitted beam in a 90° optical hybrid. In the optical hybrid, 2 beat signals with a 90° phase delay are generated, which are "I" (in-phase) and "Q" (quadrature phase), respectively. The 2 beat signals are detected by separate balanced photodetectors (BPDs) and, together with the F–P signals, are synchronously acquired by a data acquisition (DAQ) card.

As shown in Fig. 2C, both the emitted and reflected beams in the DSB-FSI system contain 2 frequency-sweep sidebands. At the same moment, the frequency difference between the 2 sidebands is less than 16 GHz, resulting in the 2 sets of interference fringes being superimposed. When the target is not stationary, variations in the optical path difference (OPD) induce a Doppler frequency shift f_d, thereby modulating the interference fringes. To eliminate dynamic magnification errors, the fringe counts corresponding to the positive and negative sidebands are averaged. Therefore, IQ demodulation is required to distinguish the interference fringes corresponding to the 2 frequency-sweep sidebands [21,22].

Measurement principle

The emitted laser of DSB-FSI system during the nth measurement can be expressed as:

$$\begin{aligned} S_{e,n}(t) &= S_{e,\text{positive},\ n}(t) + S_{e,\text{negative},n}(t) \\ &= \exp\left(2\pi i\left(f_L + f_0\right)t + \pi i K t^2\right) + \exp\left(2\pi i\left(f_L - f_0\right)_L t - \pi i K t^2\right) \end{aligned} \quad (1)$$

where $S_{e,\text{positive},n}(t)$ and $S_{e,\text{negative},n}(t)$ represent the positive and negative sidebands of the emitted laser, respectively. f_L is the frequency of the laser carrier. f_0 is the initial frequency of the linearly frequency-modulated RF signal. $t \in [0,\ T]$, where T is the duration of a single frequency sweep, and K is the frequency-sweep rate.

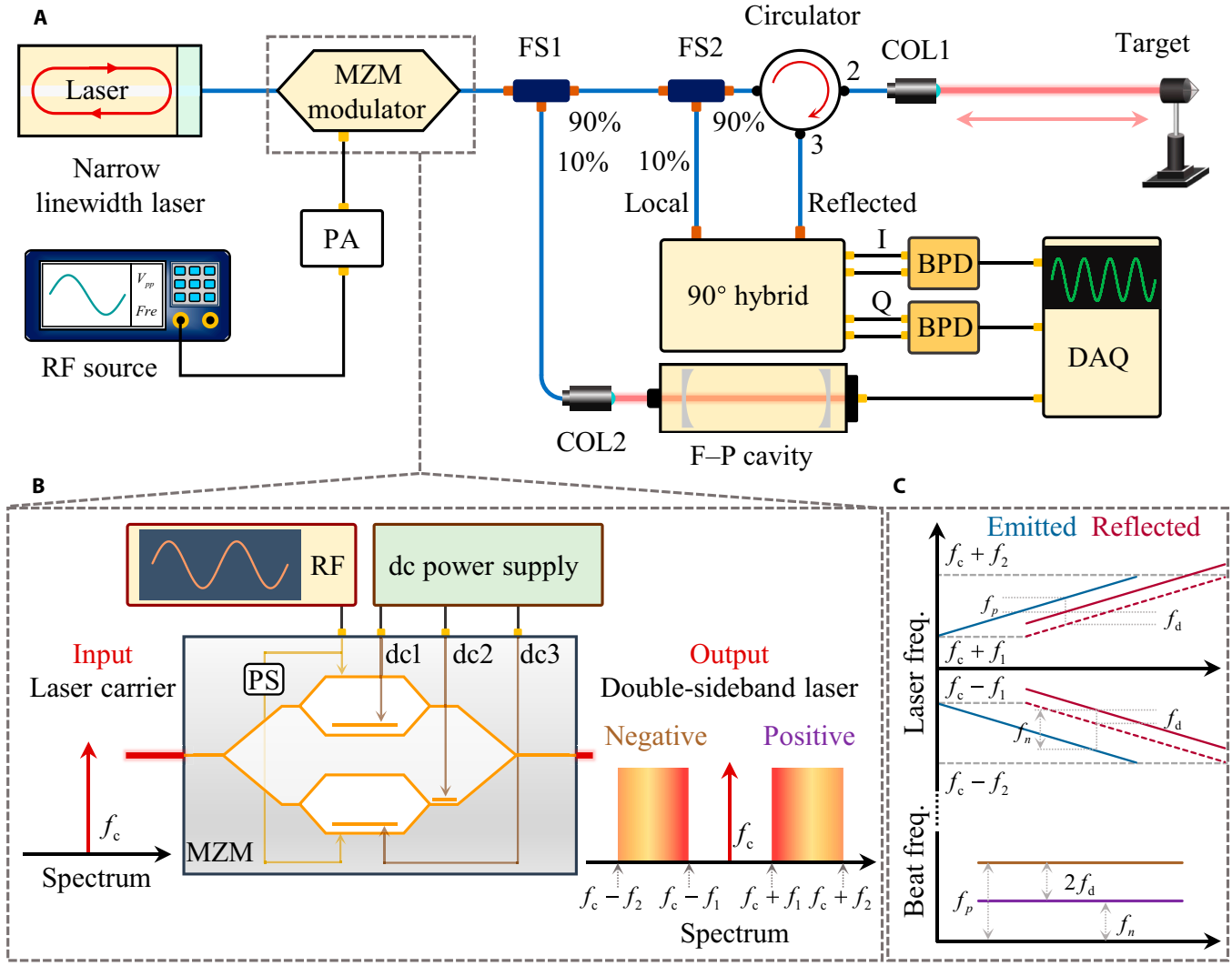

Fig. 2. (A) Schematic diagram of DSB-FSI system. (B) The double-sideband modulation principle based on the MZM. (C) Schematic diagram of the DSB-FSI interference principle. Dashed line, reflected laser frequency for a static target; solid line, reflected laser frequency for a moving target. PS, phase shifter; PA, power amplifier.

The reflected laser can be expressed as:

$$S_{r,n}(t) = S_{e.n}(t-\tau) = S_{e,n}\left(t - L_n/c\right) \tag{2}$$

where τ represents the time delay relative to the emitted laser, c is the speed of light, and L_n denotes the OPD in the nth measurement, which can be approximated as:

$$L_n = L_n(0) + v_n \cdot T \tag{3}$$

where v_n is the target velocity and $L_n(0)$ is the initial OPD in the nth measurement. The reflected laser can be written as:

$$\begin{aligned} S_{r,n}(t) &= S_{r,\text{positive},n}(t) + S_{r,\text{negative},n}(t) \\ &= \exp\left[2\pi i\left(f_L + f_0\right)\left(t - \frac{L_n(0)+2v_n t}{c}\right) + \pi i K\left(t - \frac{L_n(0)+2v_n t}{c}\right)^2\right] \\ &+ \exp\left[2\pi i\left(f_L + f_0\right)\left(t - \frac{L_n(0)+2v_n t}{c}\right) - \pi i K\left(t - \frac{L_n(0)+2v_n t}{c}\right)^2\right] \end{aligned} \tag{4}$$

The emitted and reflected laser beams interfere in the 90° optical hybrid, yielding 4 optical output signals in quadrature:

$$\begin{cases} S_1 = \frac{1}{4}A_e + \frac{1}{4}A_r - \frac{A_e A_r}{2}\left[\sin\varphi_{\text{positive}}(t) + \sin\varphi_{\text{negative}}(t)\right] \\ S_2 = \frac{1}{4}A_e + \frac{1}{4}A_r + \frac{A_e A_r}{2}\left[\sin\varphi_{\text{positive}}(t) + \sin\varphi_{\text{negative}}(t)\right] \\ S_3 = \frac{1}{4}A_e + \frac{1}{4}A_r - \frac{A_e A_r}{2}\left[\cos\varphi_{\text{positive}}(t) + \cos\varphi_{\text{negative}}(t)\right] \\ S_4 = \frac{1}{4}A_e + \frac{1}{4}A_r + \frac{A_e A_r}{2}\left[\cos\varphi_{\text{positive}}(t) + \cos\varphi_{\text{negative}}(t)\right] \end{cases} \tag{5}$$

where A_e and A_r represent the amplitudes of the emitted and reflected laser, respectively. The phases $\varphi_{\text{positive}}(t)$ and $\varphi_{\text{negative}}(t)$ correspond to the positive and negative frequency-sweep sidebands of the beat signals, respectively:

$$\begin{cases} \varphi_{\text{positive}}(t) = 2\pi\left[\left(-\frac{2Kv_n}{c} + \frac{2Kv_n^2}{c^2}\right)t^2 + \left(-\frac{L_n K}{c} - \frac{2v_n(f_L+f_0)}{c} + \frac{2L_n K v_n}{c^2}\right)t + \varphi_p\right] \\ \varphi_{\text{negative}}(t) = 2\pi\left[\left(\frac{2Kv_n}{c} - \frac{2Kv_n^2}{c^2}\right)t^2 + \left(\frac{L_n K}{c} - \frac{2v_n(f_L-f_0)}{c} - \frac{2L_n K v_n}{c^2}\right)t + \varphi_n\right] \end{cases} \tag{6}$$

where φ_p and φ_n represent the initial phases of beat signals generated by the positive and negative frequency-sweep sidebands, respectively. After photoconversion by the BPDs, the 2 orthogonal beat signals are obtained and expressed as:

$$\begin{cases} S_{\mathrm{I}}(t) = S_2 - S_1 = A_{\mathrm{I}}\left[\sin\varphi_{\mathrm{positive}}(t) + \sin\varphi_{\mathrm{negative}}(t)\right] \\ S_{\mathrm{Q}}(t) = S_4 - S_3 = A_{\mathrm{Q}}\left[\cos\varphi_{\mathrm{positive}}(t) + \cos\varphi_{\mathrm{negative}}(t)\right] \end{cases} \tag{7}$$

The amplitudes A_{I} and A_{Q} correspond to the beat signals in the 2 orthogonal paths, respectively.

In nth measurement, the phase changes of the positive and negative frequency-sweep sideband signals during the time T are expressed as follows:

$$\begin{cases} \Delta\varphi_{\mathrm{positive},\,n} = 2\pi\left[\left(\frac{2K\nu_n}{c} - \frac{2K\nu_n^2}{c^2}\right)T^2 + \left(\frac{L_nK}{c} + \underbrace{\frac{2\nu_nf_{\mathrm{L}}}{c}}_{\text{Dopplershift}} + \frac{2\nu_nf_0}{c} - \frac{2L_nK\nu_n}{c^2}\right)T\right] \\ \Delta\varphi_{\mathrm{negative},\,n} = 2\pi\left[\left(\frac{2K\nu_n}{c} - \frac{2K\nu_n^2}{c^2}\right)T^2 + \left(\frac{L_nK}{c} - \underbrace{\frac{2\nu_nf_{\mathrm{L}}}{c}}_{\text{Dopplershift}} + \frac{2\nu_nf_0}{c} - \frac{2L_nK\nu_n}{c^2}\right)T\right] \end{cases} \tag{8}$$

Equation (8) demonstrates that the error amplification caused by the Doppler shift can be canceled by averaging the phase terms $\Delta\varphi_{\mathrm{positive},\,n}$ and $\Delta\varphi_{\mathrm{negative},\,n}$, i.e.,

$$\begin{aligned} \Delta\varphi_{\mathrm{ave}} &= \frac{\Delta\varphi_{\mathrm{positive},\,n} + \Delta\varphi_{\mathrm{negative},\,n}}{2} \\ &= 2\pi\left[\left(\frac{2K\nu_n}{c} - \frac{2K\nu_n^2}{c^2}\right)T^2 + \left(\frac{L_nK}{c} + \frac{2\nu_nf_0}{c} - \frac{2L_nK\nu_n}{c^2}\right)T\right] \end{aligned} \tag{9}$$

The Doppler-induced error amplification term is determined by the difference between $\Delta\varphi_{\mathrm{positive},\,n}$ and $\Delta\varphi_{\mathrm{negative},\,n}$, i.e.,

$$\Delta\varphi_{\mathrm{diff}} = \Delta\varphi_{\mathrm{positive},\,n} - \Delta\varphi_{\mathrm{negative},\,n} = 8\pi\nu_nf_{\mathrm{L}}T/c \tag{10}$$

According to Eqs. (9) and (10), L_n, ν_n, and ΔL can be expressed as:

$$\begin{cases} L_n = \Delta\varphi_{\mathrm{ave}} \cdot c/2\pi KT \\ \nu_n = c \cdot \Delta\varphi_{\mathrm{diff}}/8\pi f_{\mathrm{L}}T \\ \Delta L = \nu_n \cdot T \end{cases} \tag{11}$$

In this study, a novel phase detection method based on the all-phase fast Fourier transform [21,22,29] is used to achieve precise extraction of the beat signal phase.

DSB-FSI frequency-sweep traceability method

The measurement precision and system reliability in DSB-FSI are directly governed by the accuracy and stability of the K. In practice, in conventional DSB-FSI systems, the K is defined as $K = B/T$, where B is the RF signal frequency-sweep bandwidth and T is the frequency-sweep time. However, maintaining a constant K is challenging due to component-dependent transmission efficiency and system noise. To overcome this limitation, we propose a dynamic frequency-sweep rate calibration method for DSB-FSI system based on an F–P etalon. When the laser enters the F–P etalon, multiple-beam interference occurs within the etalon. For single-sideband frequency-sweep laser, the transmitted laser intensity can be expressed as:

$$I_{\mathrm{T}} = I_0\frac{\left(1-R^2\right)}{\left(1-R^2\right) + 4R\sin^2\left(\frac{\varphi}{2}\right)} \tag{12}$$

where R denotes the reflectivity of the etalon mirrors, and

$$\varphi = 4\pi f_{\mathrm{L}}n_0d/c \tag{13}$$

where n_0 is the refractive index of the etalon medium and d is the cavity length of the F–P etalon. When $\frac{\varphi}{2} = k\pi$, where $k \in N+$, the resonant transmission peaks will occur.

If the incident laser beam contains both positive and negative frequency-sweep sidebands, the transmitted intensity can be expressed as:

$$\begin{aligned} I_T = {} & I_{\mathrm{negative}}\frac{\left(1-R^2\right)}{\left(1-R^2\right) + 4R\sin^2\left(\frac{\varphi_{\mathrm{negative}}}{2}\right)} \\ & + I_{\mathrm{positive}}\frac{\left(1-R^2\right)}{\left(1-R^2\right) + 4R\sin^2\left(\frac{\varphi_{\mathrm{positive}}}{2}\right)} \end{aligned} \tag{14}$$

Here, $\varphi_{\mathrm{positive}}$ and $\varphi_{\mathrm{negative}}$ represent the phases of the negative and positive sideband frequency-sweep laser in the etalon, respectively, and are given by:

$$\begin{cases} \varphi_{\mathrm{negative}} = 4\pi f_{\mathrm{L,\,negative}}n_0d/c \\ \varphi_{\mathrm{positive}} = 4\pi f_{\mathrm{L,\,positive}}n_0d/c \end{cases} \tag{15}$$

where the $\varphi_{\mathrm{positive}}$ and $\varphi_{\mathrm{negative}}$ satisfy:

$$\begin{cases} \varphi_{\mathrm{negative}} = k_1\pi\left(k_1 = 1, 2\ldots, N\right) \\ \varphi_{\mathrm{positive}} = k_2\pi\left(k_2 = 1, 2\ldots, N\right) \end{cases} \tag{16}$$

The resonance peaks appear in F–P transmission signal, and the frequency spacing between 2 adjacent peaks of the positive (or negative) sideband is defined as the free spectral range (FSR):

$$\Delta f_{\mathrm{FSR}} = c/2n_0d \tag{17}$$

Substituting Eqs. (15) and (17) into Eq. (14) yields:

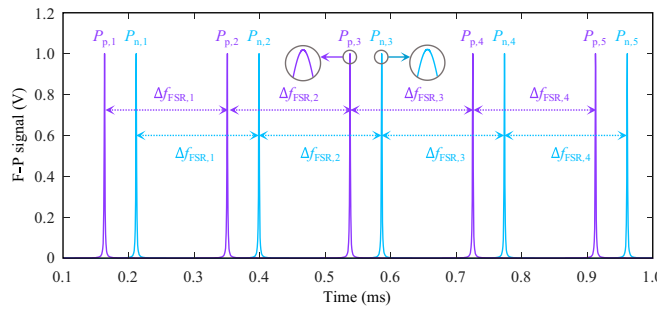

Fig. 3. Double-sideband frequency-sweep F–P signals. $P_{p,i}$ and $P_{n,i}$ denote the ith F–P resonance peak generated by the positive and negative sideband frequency-sweep signals, respectively.

$$I_T = I_{\text{negative}} \frac{\left(1-R^2\right)}{\left(1-R^2\right)+4R\sin^2\left(\pi\frac{f_{\text{L,negative}}}{\Delta f_{\text{FSR}}}\right)} + I_{\text{positive}} \frac{\left(1-R^2\right)}{\left(1-R^2\right)+4R\sin^2\left(\pi\frac{f_{\text{L,positive}}}{\Delta f_{\text{FSR}}}\right)}. \quad (18)$$

This indicates that resonance peaks occur when the incident laser frequency is an integer multiple of the FSR. Figure 3 illustrates the resonance signal generated by double-sideband frequency-sweep laser in the F–P etalon. The K_i values of the positive and negative sidebands can be expressed as:

$$\begin{cases} K_{\text{p}} = (N-1)\Delta f_{\text{FSR}}/\Delta t_{\text{FSR,p}} \\ K_{\text{n}} = (N-1)\Delta f_{\text{FSR}}/\Delta t_{\text{FSR,n}} \end{cases} \quad (19)$$

where N is the number of generated double-sideband F–P signal groups and $\Delta t_{\text{FSR, p}}$ and $\Delta t_{\text{FSR, n}}$ denote the time intervals

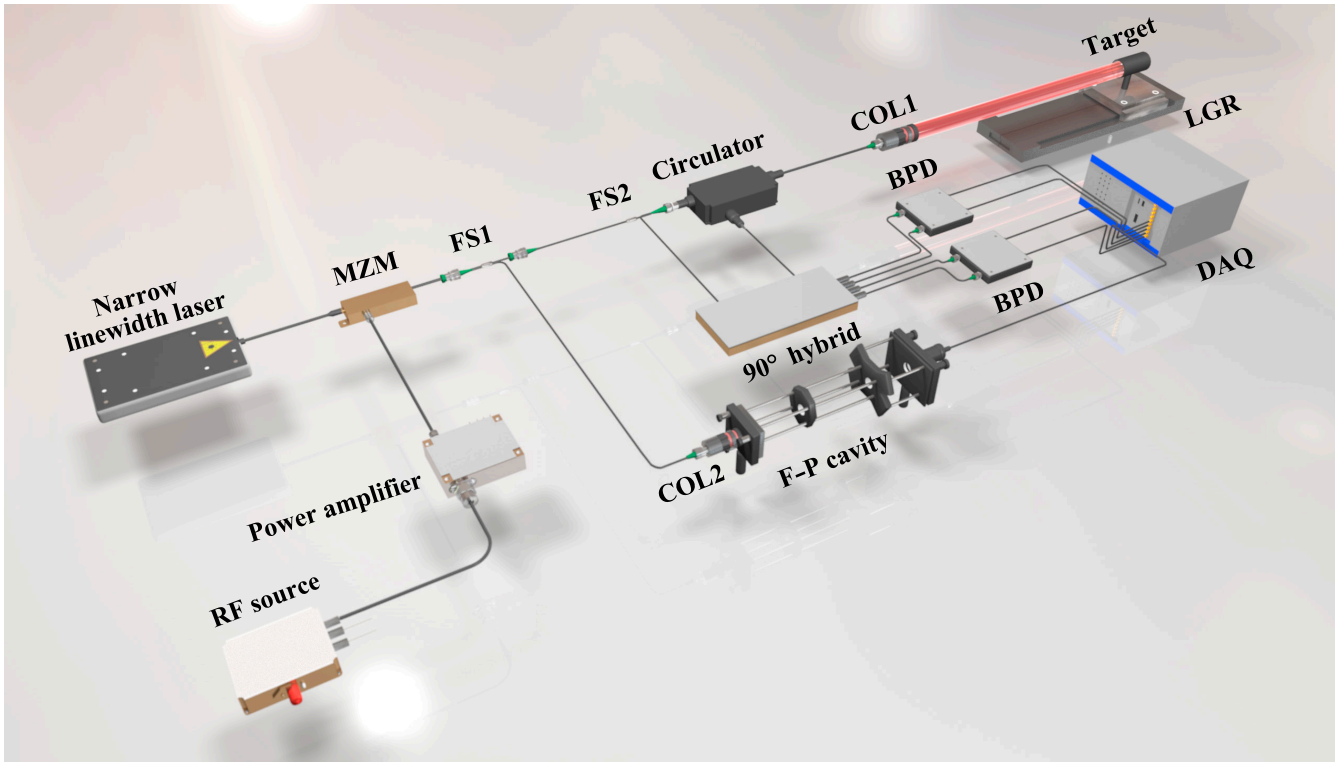

Fig. 4. DSB-FSI experimental system.

Table 1. Specific parameters of the experimental devices

Device name	Manufacturer	Parameters
Laser	Femto Technology (Xi'an)	Wavelength: 1,550.12 ± 0.1 nm; linewidth: <3 kHz; power: 20–30 mW
BPD	Femto Technology (Xi'an)	Responsivity: 0.95 A/W at 1,550 nm; bandwidth: <100 MHz; wavelength: 800–1,700 nm
RF source	NF Wave Factory	Frequency range: 8–16 GHz; step size: 100 Hz; sweep time: 1 ms
Power amplifier	iXblue	Gain: 27 dB; saturate output power: 28 dBm
MZM	iXblue	Usable electro-optical bandwidth: 16 GHz
FS	Thorlabs	Center wavelength: 1,550 nm; bandwidth: ± 15 nm
COL	Thorlabs	f = 6–18 mm; numerical aperture = 0.25; wavelength: 1,050–1,650 nm
Circulator	Thorlabs	Wavelength: 1,530–1,570 nm; isolation: 32 dB
F–P cavity	Thorlabs	FSR: 1.5 GHz; resolution: 7.5 MHz
RR	Thorlabs	Reflectance per surface: >97% for 800 nm–20 μm
LGR	Newport	Repeatability: ±0.12 μm; resolution: 10 nm
90° optical hybrid	Optoplex	Phase shit accuracy between I and Q: ±10°
DAQ	National Instruments	Single-channel sampling rate: <60 MHz

between the first and last resonance peaks for the positive and negative sideband F–P signals, respectively. The system frequency-sweep rate K is defined as the average of the positive and negative sidebands frequency-sweep rates:

$$K = \left(K_p + K_n\right)/2 \tag{20}$$

The F–P etalon enables real-time frequency-sweep rate monitoring, providing a stable reference for DSB-FSI systems.

Results

DSB-FSI system measurement performance

To evaluate the measurement performance of the DSB-FSI system, we established an experimental system, as shown in Fig. 4. The specific parameters of the experimental setup are detailed in Tables 1 and 2, respectively. The target retroreflector (RR) was mounted on a linear guided rail (LGR; Newport, M-ILS200LM-S; bidirectional repeatability: ±0.12 μm) and moved in 1-mm increments. Distance measurements were performed at 11 different positions, with each position $P_i (i = 0,1,\ldots,10)$ measured for 0.5 s. The measurement results are shown in Fig. 5A. At different positions, the SDs of the distance results obtained by single-sideband (positive or negative sideband) are substantially higher than those obtained with DSB-FSI. Moreover, as shown in Fig. 5B, the maximum SDs for the positive and negative sidebands are 175.78 and 179.14 μm, respectively, while the maximum SD for the DSB-FSI measurement is only 2.38 μm. Fig. 5C presents the mean values of 500 measurements at each position, with the total displacement from P_0 to P_{10} being 10 mm. Within this range, when the target moves in equal 1-mm intervals, the displacement linearity coefficients are 0.99779 (positive sideband), 0.99772 (negative sideband), and 0.99998 (double sideband), respectively. Correspondingly, as shown in Fig. 5D, the maximum absolute deviation relative to the 1-mm standard value are −368.34, 406.38, and −18.82 μm, respectively. These results indicate that,

Table 2. The experimental environmental parameters

Item	Temperature /°C	Atmospheric pressure /kPa	Humidity/(% relative humidity)	Vibration
Value	24 ± 0.25	101.325 ± 2.5	45 ± 0.16	Vibration isolation

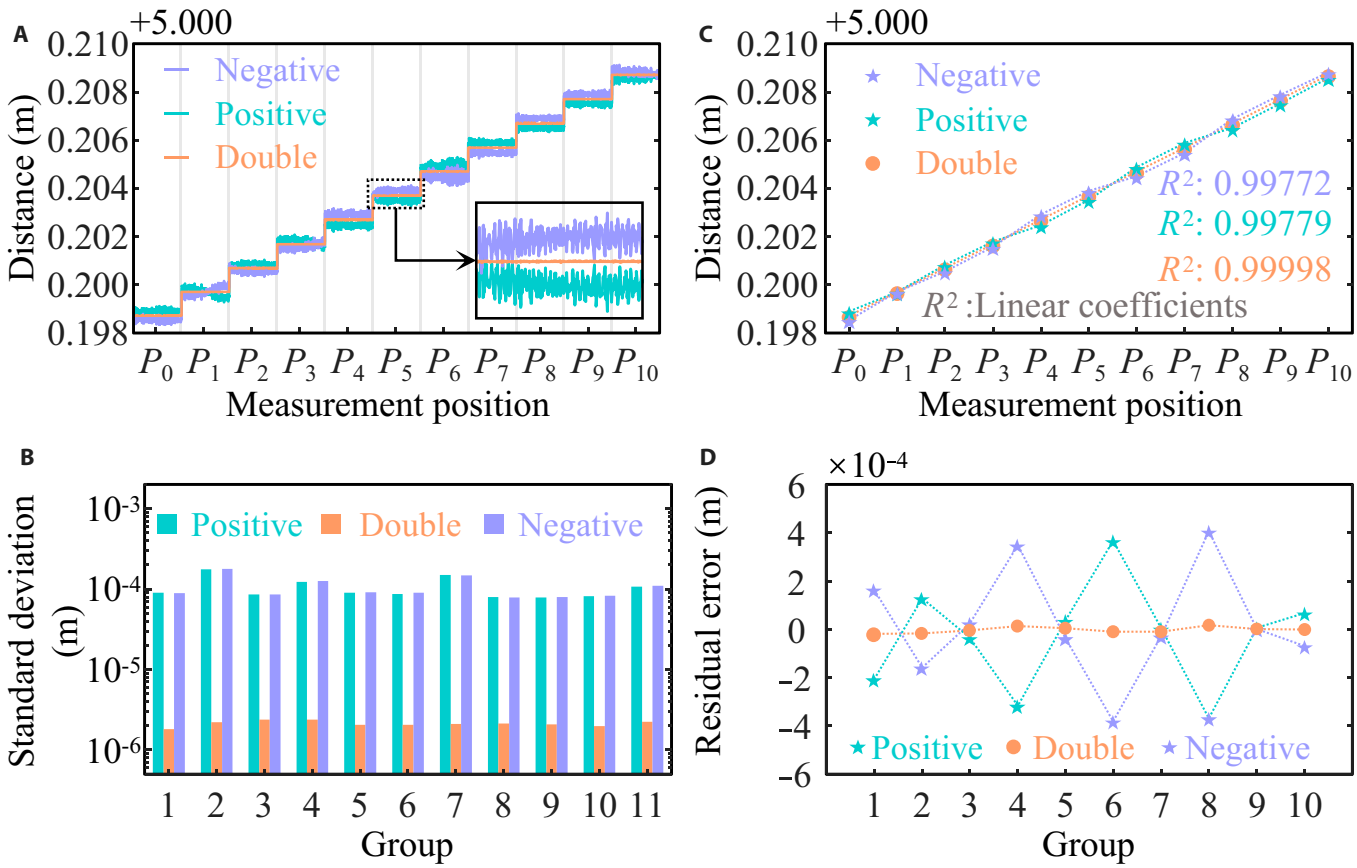

Fig. 5. (A) Distance measurement results with a step of 1 mm at 11 different positions. (B) SD of the distance measurement results. (C) Displacement curve with equal intervals of 1-mm steps. (D) Measurement deviation relative to the standard value.

within the same measurement range, the DSB-FSI system achieves higher repeatability and measurement accuracy.

Frequency-sweep rate calibration and distance measurement

To assess the performance enhancement achieved through K calibration, the DSB-FSI system continuously measured distance over a 1-h period on a 5.7-m baseline. As shown in Fig. 6A, when K is the system default value (8×10^{12} Hz/s) for distance measurement, the range of distance fluctuations was 20.11 μm. The K value was simultaneously monitored by an F–P etalon, as shown in Fig. 6B. After compensating the distance values using the measured K, the fluctuation range decreased to 13.38 μm, as shown in Fig. 6C. Figure 6D presents the distribution of long-term distance deviations before and after K calibration. Before calibration, deviations were mainly within ±10 μm, whereas after calibration, they were concentrated within ±5 μm. These results indicate that K calibration considerably improves the long-term stability of the DSB-FSI system and suppresses distance drift caused by fluctuations in K.

To further analyze the impact of K calibration on distance measurement accuracy, we used the system shown in Fig. 4 for additional experiments. Unlike previous tests, the LGR was moved in 50-mm increments over a 200-mm range. The time interval between consecutive measurements was approximately 10 min. The distance measurement results using the default K value and the F–P etalon-calibrated K value are shown in Figs. 7A and B, respectively. The displacement deviations relative to the standard 50 mm, both before and after K calibration, are presented in Fig. 7C. Over an approximate 40-min period, the DSB-FSI system recorded maximum displacement measurement deviations of 18.03 μm before K calibration and 13.14 μm after K calibration, respectively. These experimental results demonstrate that K calibration consistently reduces measurement deviations at each interval, thereby indicating that this approach effectively enhances the distance measurement accuracy for the DSB-FSI system.

Metrology and verification for the DSB-FSI system

The integrated DSB-FSI system's distance measurement accuracy was assessed at the Xi'an Aerospace Institute of Metrology and Measurement. The metrological setup is shown in Fig. 8A, where the LGR has a travel range of 10 m and the target RR is mounted on the stage carriage. The DSB-FSI system performed forward measurements of the target RR, while a He–Ne laser interferometer (Renishaw XL-80; linear positioning accuracy ≤ 0.5 ppm and long-term stability ≤ 0.6×10^{-7}) simultaneously measured from the opposite side of the target RR to provide a high-precision reference. The distance measured by the DSB-FSI system at each position P_i is denoted as $L_i (i = 0,1,2, \ldots ,10)$, and the displacement relative to the starting position is given by:

$$D_i = L_i - L_0 \tag{21}$$

The displacement measurement results from the DSB-FSI system and the Renishaw laser interferometer are shown in Fig. 8B, and the measurement deviations are presented in Fig. 8C, with a maximum deviation of 44.30 μm and a minimum deviation of

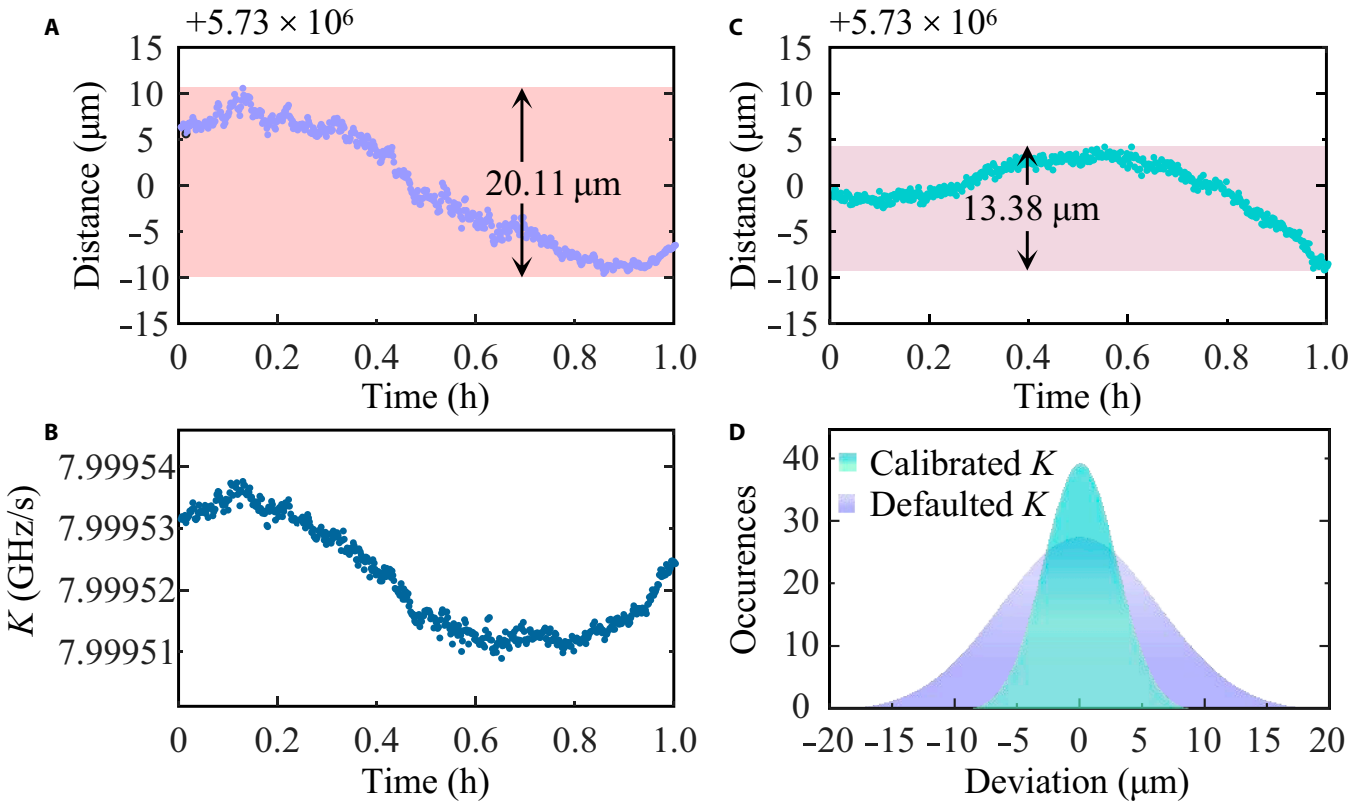

Fig. 6. (A) Distance results measured using the system-set K value. (B) The real-time measured K by the F–P etalon. (C) Distance values calibrated using the measured K. (D) Normal distribution of distance measurement deviations (Gaussian fitting).

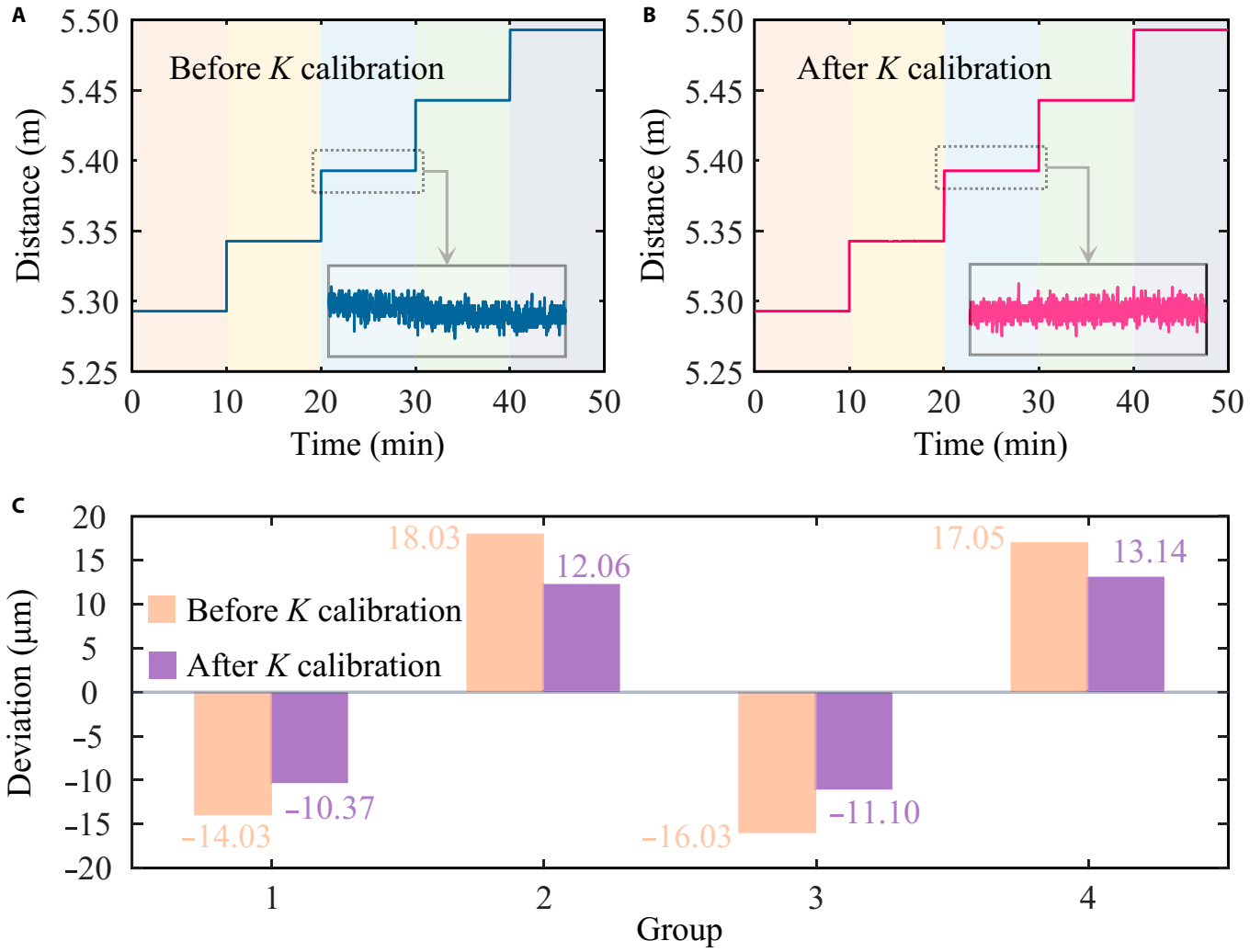

Fig. 7. (A) Distance measurement results before *K* calibration. (B) Distance measurement results after *K* calibration. (C) Comparison of measurement deviations before and after *K* calibration.

10.80 μm. Detailed measurement data are listed in Table 3. These results demonstrate that the proposed DSB-FSI system achieves excellent distance measurement accuracy.

To evaluate the dynamic measurement capability of the DSB-FSI system, we used the LGR (as shown in Fig. 8A) to test its velocity measurement accuracy. The LGR was programmed to move at velocities of 5, 10, 15, and 20 mm/s, maintaining uniform motion for 1 s at each speed. As shown in Fig. 9A, the linearity coefficients R^2 for the displacement of target RR under all speeds exceed 0.99999. Figure 9B presents the measured target velocities, while Fig. 9C shows the corresponding velocity measurement deviations. A maximum deviation was −16.80 μm/s was observed, occurring at a velocity of 20 mm/s.

In addition, the vibration measurement capability of the DSB-FSI system was evaluated using the experimental setup illustrated in Fig. 10A. The target RR was mounted on a piezoelectric translation stage, actuated by an external signal to induce vibration. The vibration output from the piezoelectric translation stage served as the reference for assessing the vibration measurement accuracy. As shown in Fig. 10B, the vibration amplitude measured by the DSB-FSI system was 0.54 μm, closely matching the reference values from the piezoelectric translation stage. The relative error between the measured and reference values is presented in Fig. 10D, with a local maximum error of 0.05 μm (9.26%) and an overall mean error of 0.02 μm (3.70%). The frequency spectra of both measurements are shown in Fig. 10C: The system measured a vibration frequency of 200.78 Hz, while the piezoelectric translation stage output was 200.59 Hz, yielding a frequency measurement error below 0.2 Hz and a relative error of approximately 0.10%.

The vibration measurement results obtained from both the piezoelectric translation stage and the DSB-FSI system at different frequencies are summarized in Table 4. The amplitude residual error was less than 0.08 μm, and the corresponding relative error was below 3.72%. These dynamic experimental results demonstrate that the DSB-FSI system, equipped with an F–P etalon, exhibits excellent performance in both simultaneous velocity and vibration measurements.

Discussion

The DSB-FSI technology is currently in the ground-based experimental validation stage. Its on-orbit application still faces critical technical challenges. In the space environment, temperature

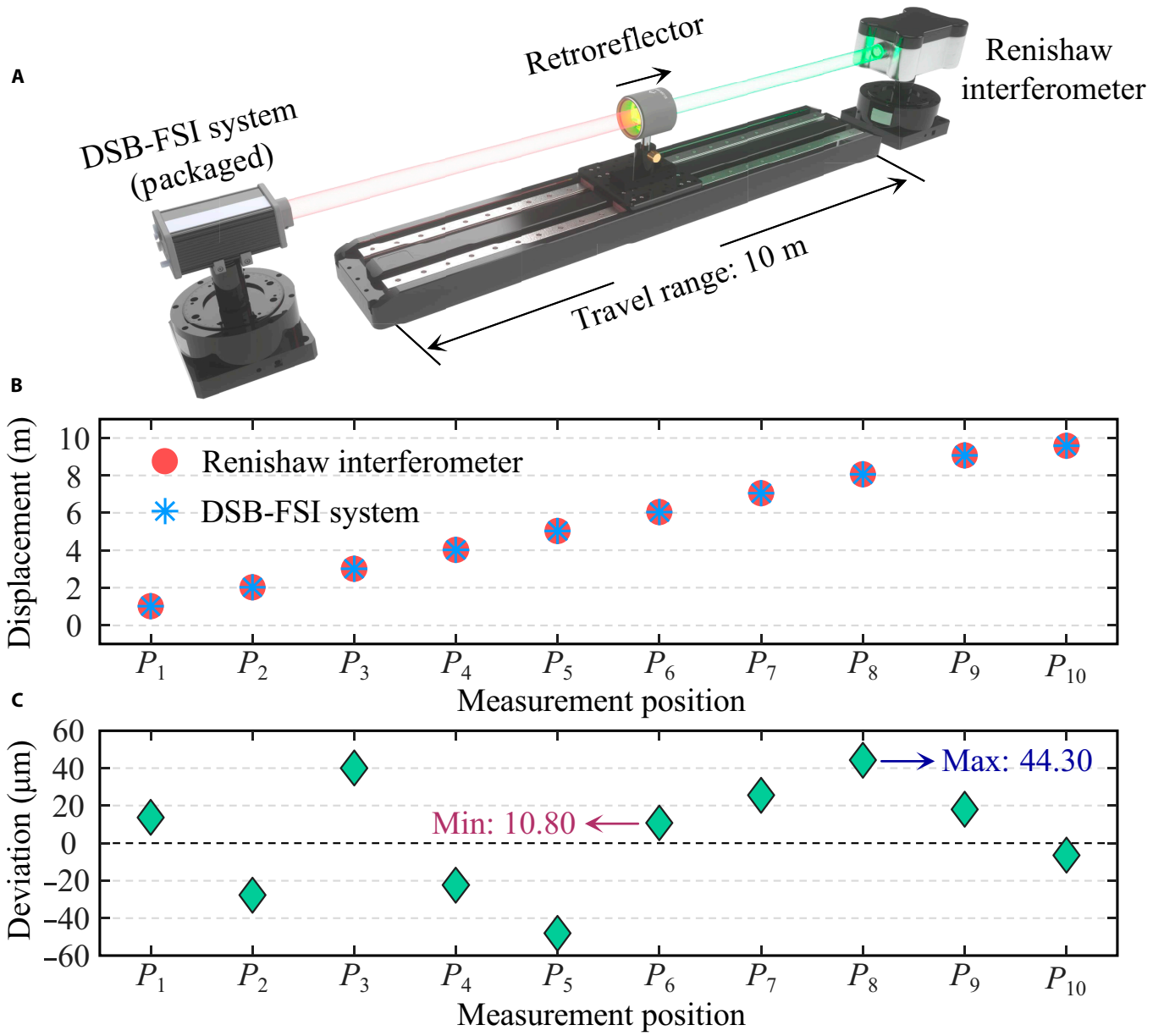

Fig. 8. Distance accuracy metrological calibration system. (B) Distance measurement results of the DSB-FSI system and the Renishaw laser interferometer. (C) Measurement deviations of the DSB-FSI system relative to the Renishaw laser interferometer.

fluctuations, radiation, and microgravity can impair laser stability, damage electronic components, and reduce optical alignment accuracy, thereby limiting ranging accuracy and long-term reliability.

Beyond these environmental factors, system-level error sources also play a critical role. This study primarily analyzes the effect of frequency-sweep rate fluctuations on system stability and measurement accuracy. Nevertheless, in the complete measurement chain, additional error sources remain, including laser stability, optical system performance, signal detection and sampling precision, and environmental disturbances. These errors may manifest in the beat signal as noise or modulation, thereby degrading the accuracy of distance measurements.

For future on-orbit applications, this technology requires targeted optimization in active thermal control, radiation hardening, vibration isolation, and microgravity compensation. Based on a comprehensive analysis of error sources, system robustness and environmental adaptability should be enhanced through hardware improvements and algorithmic refinements. While the experiments in this study were conducted on 5.7- and 10-m baselines, extending the range to hundreds of meters will require high-efficiency optical antennas and precise pointing, acquisition, and tracking systems to maintain stable return optical power. Overall, numerous engineering and technical challenges remain to be addressed before DSB-FSI technology can be reliably applied on orbit.

Summary and conclusion

In summary, this study addresses the high-precision baseline measurement requirements for space-based distributed array telescope formations by proposing a method based on DSB-FSI technology. The work focuses on overcoming the lack of traceable

Table 3. Measurement results of the DSB-FSI system and the Renishaw interferometer

Number	Reference value/mm	Measured value/mm	Deviation/mm
1	1,021.8960	1,021.9098	+0.0138
2	2,023.6890	2,023.6613	−0.0277
3	3,024.5600	3,024.6001	+0.0401
4	4,030.5210	4,030.4986	−0.0224
5	5,037.0650	5,037.0169	−0.0481
6	6,043.9810	6,043.9918	+0.0108
7	7,051.4500	7,051.4756	+0.0256
8	8,059.0550	8,059.0993	+0.0443
9	9,066.4770	9,066.4951	+0.0181
10	9,580.4780	9,580.4716	−0.0064

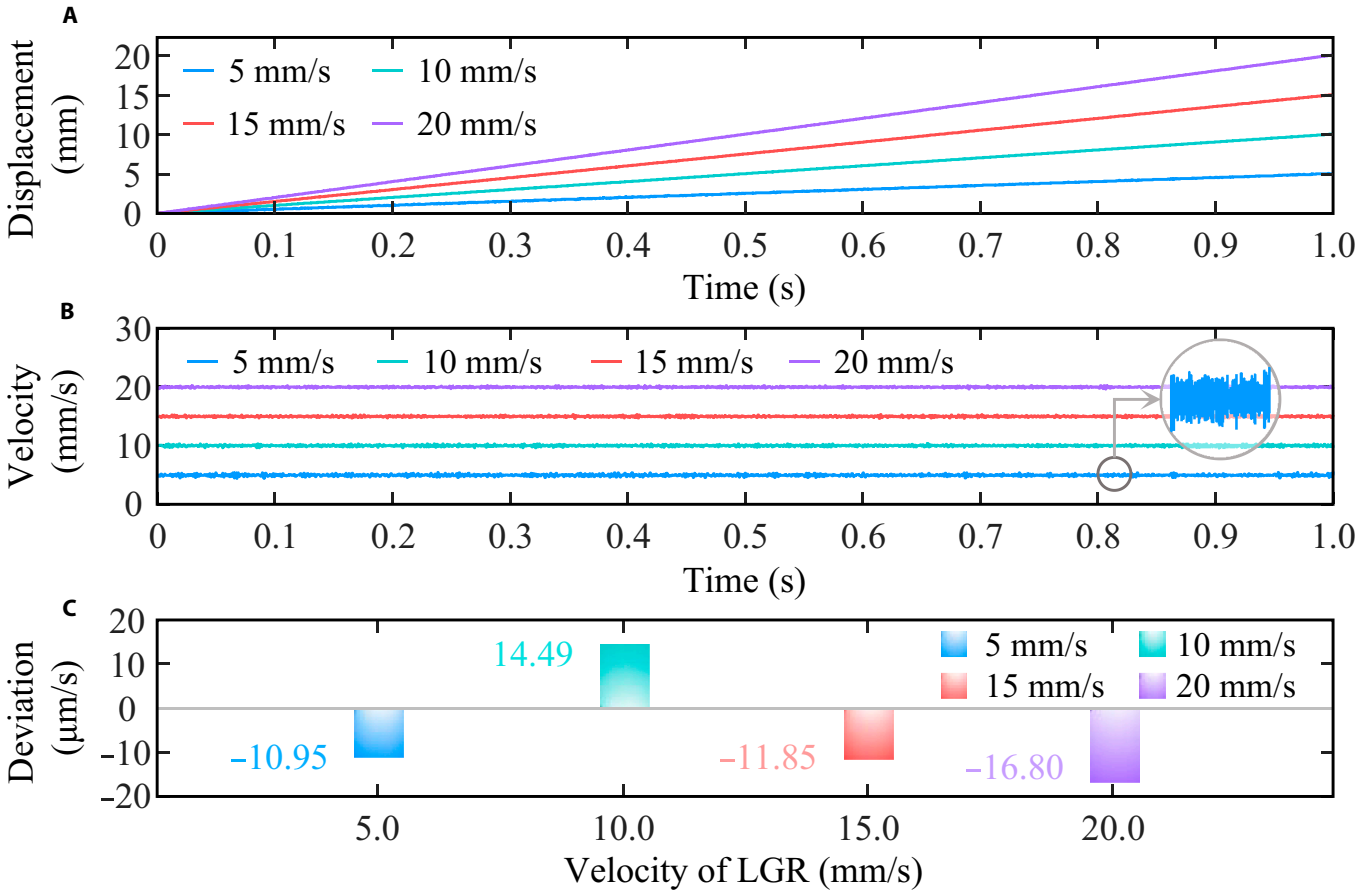

Fig. 9. (A) Displacement measurement results. (B) Measurement results at different velocities. (C) Velocities measurement deviation.

on-orbit references in this technique, particularly the challenge of frequency-sweep rate calibration. To address this issue, an innovative on-orbit calibration method utilizing an F–P etalon is introduced. Experimental results demonstrate that the proposed method effectively suppresses long-term drift in frequency-sweep rate, reducing the measurement error from 20.11 to 13.38 μm and improving stability by 33.47%. Further metrological verification confirms that the calibrated system exhibits superior performance in distance, velocity, and vibration measurements. Nevertheless, this method still faces 2 major technical issues:

1. Spatial resolution of the F–P signal: Within the 8-GHz frequency-sweep bandwidth, the number of resonance

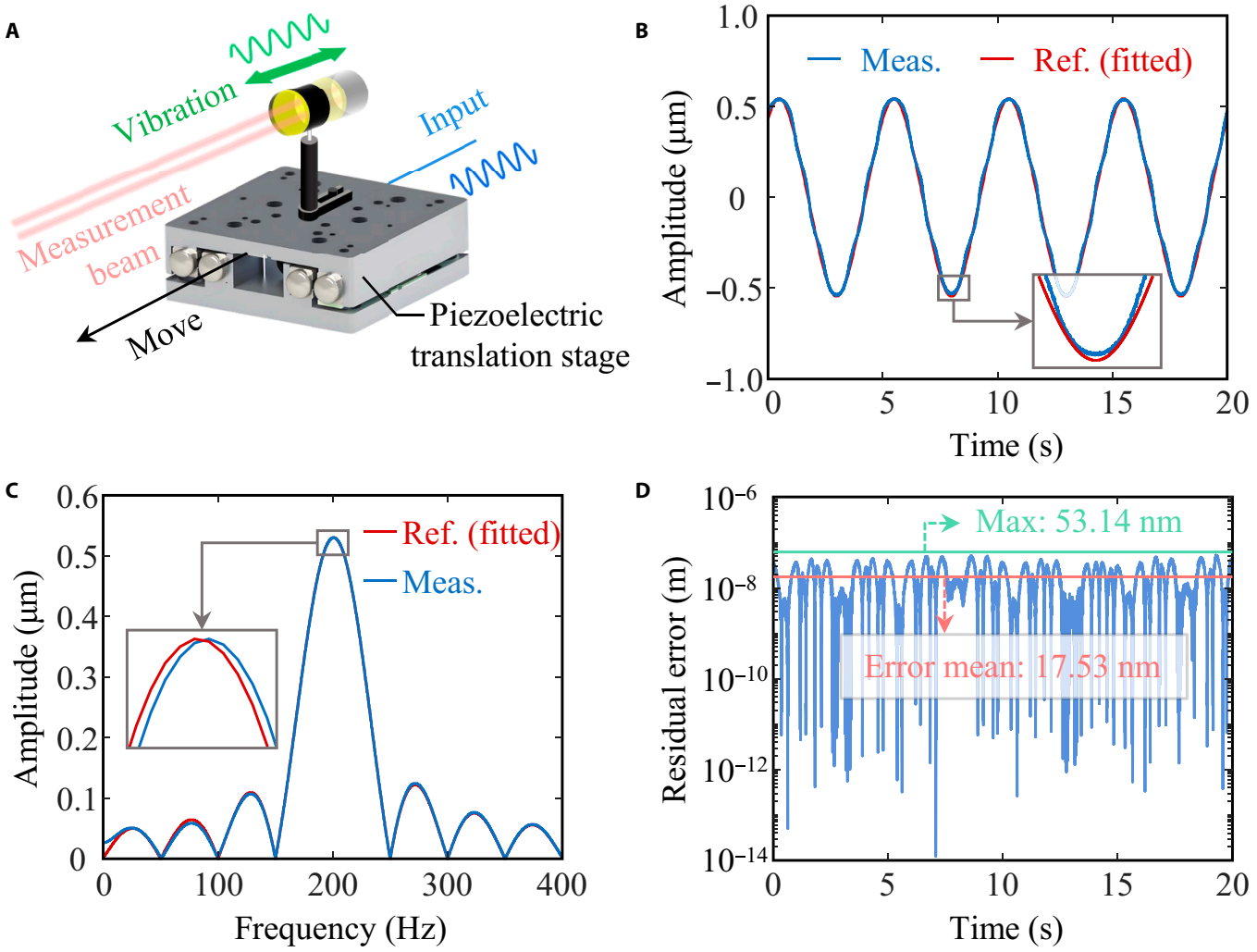

Fig. 10. (A) Vibration experiment setup. (B) Comparison between system measurements and translation stage outputs. (C) Spectra of vibration measurements and reference values. (D) Measurement residuals relative to the reference values.

Table 4. Results of vibration measurements at different frequencies

Vibration frequency/Hz	50	100	200	500
Piezoelectric translation stage/μm	2.17	1.82	0.67	0.48
DSB-FSI/μm	2.09	1.75	0.63	0.45
Error/μm	0.08	0.07	0.04	0.03
Relative error/%	3.72	3.83	3.90	4.01

peaks generated by the F–P etalon for frequency-sweep rate determination is limited.

2. Accuracy of F–P peak position extraction: The F–P signal profile may be affected by incident light intensity fluctuations and fitting errors, which can reduce the accuracy of peak position determination.

Although alternative approaches such as optical frequency combs, gas absorption cells, and *k*-clock techniques can also provide traceability and frequency-sweep rate calibration, the F–P etalon offers advantages in terms of compact structure and high stability, making it more suitable for on-orbit applications. Future research may further improve the performance of on-orbit frequency-sweep rate calibration:

1. Designing the F–P cavity with smaller FSRs to generate more resonance peaks within a narrower frequency-sweep bandwidth
2. Developing higher-precision algorithms for peak position extraction to enhance frequency calibration accuracy
3. Integrating the advantages of gas absorption cells, *k*-clock, and F–P etalons to explore combined calibration approach

The proposed DSB-FSI system, equipped with an on-orbit frequency-sweep traceability reference, demonstrates promising potential for intersatellite baseline measurements and is expected to be implemented in the "MEAYIN" project.

Acknowledgments

Funding: This work was supported by the National Natural Science Foundation of China (nos. 52205576 and 12204409), Optoelectronic Measurement and Intelligent Perception

Zhongguancun Open Lab (no. LabSOMP-2023-04), Key Research and Development Program of Shaanxi (program no. 2025CY-YBXM-121), Fundamental Research Funds for the Central Universities (grant no. ZYTS25250), State Key Laboratory for Manufacturing Systems Engineering (grant no. klms2021005), and Natural Science Basic Research Program of Shaanxi (no. 2025JC-YBMS-016).

Author contributions: W.C. and Z.D. contributed to the data curation and methodology and wrote the original draft. X.L. and Z.D. contributed to the funding acquisition and project administration. Z.D. and H.S. contributed to the literature review and conceptualization. C.W. and S.Z. contributed to the software and data curation. H.Z., L.L., and L.W. contributed to project administration. H.G., H.K., and G.V. performed the literature review and principle. W.B. contributed to the project administration.

Competing interests: The authors declare that they have no competing interests.

Data Availability

The data used to support the findings of this study are available from the author upon reasonable request.

References

1. Jia F, Li X, Huo Z, Qiao D. Mission design of an aperture-synthetic interferometer system for space-based exoplanet exploration. *Space Sci Technol*. 2022;2022:Article 9835234.
2. Cockell CS, Léger A, Fridlund M, Herbst TM, Kaltenegger L, Absil O, Beichman C, Benz W, Blanc M, Brack A, et al. *Darwin*—A mission to detect and search for life on extrasolar planets. *Astrobiology*. 2009;9(1):1–22.
3. Fridlund CVM. The DARWIN project - An ESA cornerstone candidate mission. *Proc Int Astronom Union*. 2004;202:451–454.
4. Zhang N, Wu D, Zhang Z, Li H, Baoyin H. Preliminary trajectory design of implementing the asteroid rendezvous and impact in a single launch. *Aerosp Sci Technol*. 2025;159:Article 109959.
5. Stapelfeldt K, Beichman C, Kuchner M. General astrophysics with the optical terrestrial planet finder mission. *New Astron Rev*. 2005;49(7–9):396–399.
6. Chen W, Li X, Deng Z, Zhang S, Sun H, Li L, Zhang H, Wang L, Gong H, Koara H, et al. A phase jump phenomenon within the beat signal for dynamic target measurement in frequency-sweeping interferometry. *Appl Phys Lett*. 2025;127(8):Article 081103.
7. Cabral A, Abreu M, Rebordão JM. Dual-frequency sweeping interferometry for absolute metrology of long distances. *Opt Eng*. 2010;49(8):Article 085601.
8. Wang Z, Guo J, Tian K, Yu Y, Liu Z. Speckle noise detection and correction for frequency scanning interferometry in vibration measurement. *Measurement*. 2024;236:Article 115065.
9. Zhang F, Yi L, Qu X. Simultaneous measurements of velocity and distance via a dual-path FMCW lidar system. *Opt Commun*. 2020;474:Article 126066.
10. Lu C, Liu G, Liu B, Chen F, Gan Y. Absolute distance measurement system with micron grade measurement uncertainty and 24 m range using frequency scanning interferometry with compensation of environmental vibration. *Opt Express*. 2016;24(26):30215–30224.
11. Cheng X, Liu J, Zhang Y, Zhang F, Qu X. Simultaneous measurement of distance and speed via frequency-modulated continuous-wave LIDAR system based on $H^{13}C^{14}N$ gas cell. *Opt Lasers Eng*. 2022;159:Article 107193.
12. Gan Y, Duan C, Liu G, Liu B, Chen F. Dynamic frequency scanning interferometry measurement based on optical frequency synchronous motion measurement and error compensation. *Opt Commun*. 2021;488:Article 126753.
13. Chen W, Li X, Deng Z, Sun H, Zhang S, Liu Y, Gong H. Data-driven model based self-adaptive frequency-sweeping linearization in frequency-sweeping interferometry for absolute distance measurement. *Measurement*. 2025;253:Article 117742.
14. Bao R, Duan F, Fu X, Yu Z, Liu W, Guo G. Frequency-scanning interferometry for axial clearance of rotating machinery based on speed synchronization and extended Kalman filter. *Opt Lasers Eng*. 2023;164:Article 107515.
15. Zhang X, Pouls J, Wu MC. Laser frequency sweep linearization by iterative learning pre distortion for FMCW LiDAR. *Opt Express*. 2019;27(7):9965–9974.
16. Li Q, Liu Z, Jing T. Demodulation method for composite modulation caused by dynamic optical path in FSI optical frequency tuning. *Opt Lasers Eng*. 2022;154:Article 107011.
17. Tao L, Liu Z, Zhang W, Zhou Y. Frequency-scanning interferometry for dynamic absolute distance measurement using Kalman filter. *Opt Lett*. 2014;39(24):6997–7000.
18. Deng Z, Chen W, Li L, Sun H, Zhang H, Shen L, Gong H, Wang L, Li X. Decoupling composite modulation models in frequency-scanning interferometry for dynamic absolute ranging using a multi-synchrosqueezing transform. *Appl Opt*. 2025;64(13):3554–3560.
19. Kamata M, Hinakura Y, Baba T. Carrier-suppressed single sideband signal for FMCW LiDAR using a Si photonic-crystal optical modulators. *J Lightwave Technol*. 2020;38(8):2315–2321.
20. Xu Z, Tang L, Zhang H, Pan S. Simultaneous real-time ranging and velocimetry via a dual-sideband chirped lidar. *IEEE Photon Technol Lett*. 2017;29(24):2254–2257.
21. Zhang K, Lv T, Mo D, Wang N, Wang R, Wu Y. Double sideband frequency scanning interferometry for distance measurement in the outdoor environment. *Opt Commun*. 2018;425:176–179.
22. Mo D, Wang R, Li GZ, Wang N, Zhang KS, Wu YR. Double-sideband frequency scanning interferometry for long-distance dynamic absolute measurement. *Appl Phys B*. 2017;123(11):Article 272.
23. Dong Y, Zhu Z, Tian X, Qiu L, Ba D. Frequency-modulated continuous-wave LIDAR and 3D imaging by using linear frequency modulation based on injection locking. *J Lightwave Technol*. 2021;39(8):2275–2280.
24. Prellinger G, Meiners-Hagen K, Pollinger F. Dynamic high-resolution spectroscopic frequency referencing for frequency sweeping interferometry. *Surf Topogr Metrol Prop*. 2016;4(2):Article 024012.
25. Zhu Z, Wu G. Dual-comb ranging. *Engineering*. 2018;4(6):772–778.
26. Dale J, Hughes B, Lancaster AJ, Lewis AJ, Reichold AJH, Warden MS. Multi-channel absolute distance measurement system with sub ppm-accuracy and 20 m range using frequency scanning interferometry and gas absorption cells. *Opt Express*. 2014;22(20):24869–24893.
27. Lin C, Wang Y, Xu X, Wang Y, Hua Z, Sun H, Cao L, Tan Y. Hybrid frequency modulation LiDAR: Multi-functional measurement of absolute distance,

velocity, vibration and imaging. *J Lightwave Technol*. 2025;43(14):6662–6670.
28. Lu Z, Yang T, Li Z, Guo C, Wang Z, Jia D, Ge C. Broadband linearly chirped light source with narrow linewidth based on external modulation. *Opt Lett*. 2018;43(17):4144–4147.
29. Zhang S, Li X, Sun H, Deng Z, Chen W, Shen L, Li L, Zhang H, Wang L. Laser heterodyne interferometry nano-displacement measurement based on an electro-optic modulation double sideband. *Opt Lett*. 2025;50(13): 4274–4277.

Space: Science & Technology
A SCIENCE PARTNER JOURNAL

Frequency-Sweeping Interferometry for Intersatellite Baseline Metrology in Array Telescope Formation

Wenjun Chen, Xiaoping Li, Zhongwen Deng, Chenxu Wang, Shuwei Zhang, Haifeng Sun, Hengkang Zhang, Lin Li, Li Wang, Hai Gong, Herman Koara, Gleb Vdovin, and Weimin Bao

Citation: Chen W, Li X, Deng Z, Wang C, Zhang S, Sun H, Zhang H, Li L, Wang L, Gong H, et al. Frequency-Sweeping Interferometry for Intersatellite Baseline Metrology in Array Telescope Formation. *Space Sci Technol*. 2026;**6**:0482. DOI: 10.34133/space.0482

Space-based distributed array telescope formations hold substantial potential for deep space exploration, with their performance highly dependent on precise baseline measurements between subtelescopes. This study presents a double-sideband frequency-sweeping interferometry (DSB-FSI) technique based on electro-optic modulation for intertelescope baseline measurements. To address the lack of on-orbit frequency-sweep calibration references, a Fabry–Pérot etalon is used for real-time in situ frequency-sweep rate calibration. Experimental results show that the Fabry–Pérot etalon effectively calibrates the frequency-sweep rate of the DSB-FSI system, reducing long-term baseline measurement drift error from 20.11 to 13.38 μm and decreasing maximum measurement deviation from 18.03 to 13.14 μm over a 5.7-m baseline. Metrological calibration confirms that the calibrated system achieves a baseline measurement accuracy of 44.30 μm over a 10-m range, with excellent dynamic measurement performance for monitoring baseline variations. The DSB-FSI technique is expected to provide a reliable solution for the high-precision intertelescope baseline measurements in “MEAYIN” (Multiple-Spacecraft Exoplanet Aperture Synthetic Interferometer) project, thus supporting the advancement of space-based distributed array telescope formation technologies.
Image

Space: Science & Technology (ISSN 2692-7659) is published by the American Association for the Advancement of Science. 1200 New York Avenue NW, Washington, DC 20005.